RSC Advances

ROYAL SOCIETY OF CHEMISTRY

www.rsc.org/advances

Journal Name

RSCPublishing

ARTICLE

Structural study of hybrid silica bilayers from "bola-amphiphile" organosilane precursors: catalytic and thermal effects.

Cite this: DOI: 10.1039/x0xx00000x

Received ooth January 2012,
Accepted ooth January 2012

DOI: 10.1039/x0xx00000x

www.rsc.org/

Romain Besnard, Guilhem Arrachart*, Julien Cambedouzou*, and Stéphane Pellet-Rostaing

Hybrids materials are obtained upon acid or base-catalyzed hydrolytic condensation of bola-amphiphile organosilanes such as amino-undecyl-triethoxysilane and amino-oxy-undecyl-triethoxysilane. The self-assembling process of the amphiphile organosilanes is described at the light of several experimental techniques involving small angle X-ray scattering, light scattering, Raman, solid-state NMR and thermal analysis. The structural features of the nanostructured organic/inorganic hybrids are discussed as a function of catalytic and thermal effects. Lamellar assemblies were systematically observed, albeit with different structural evolutions during the densification mechanism depending on the catalytic conditions.

Introduction

Controlling the nanostructure, composition and morphology of hybrid silica is of great interest in order to design materials which can be used in a wide variety of applications such as catalysis,[1–3] remediation,[4–8] non-linear optical properties,[9–11] biomaterials,[12–14] or solid/liquid extraction and liquid waste processing.[15,16]

Shape-controlled hybrids are usually obtained from a surfactant-mediated pathway. Therefore, functional mesoporous materials and functionalized periodic mesoporous organosilicas (PMOs) have been synthesized using surfactants as structuring agents.[17] It has also been shown that organosilanes without amphiphilic properties could auto-associate through the hydrogen-bonding interactions between their organic units and result in a final solid material without external structuring agent.[18] Alternatively, structured hybrid silica can be achieved by using amphiphlic organosilane precursors. Based on their amphiphilic properties, such organosilica precursors could be hydrolyzed to spontaneously give structured materials without requiring further addition of external surfactant. Such an approach was already proposed in a few studies.[19–22] The self-assembly of a simple amine (amino-undecyl-triethoxysilane) had been previously studied in pentane and with CO_2 as assembly agent.[23] Recently, we described the self-assembly of this precursor as a model system for the design of organic-inorganic hybrid materials and we found that it could lead to hexagonal structures under given conditions.[24]

The aim of the present study is to determine the parameters governing the organization of amphiphilic organosilane molecules such as amino-undecyl-triethoxysilane (P1) and amino-oxy-undecyl-triethoxysilane (P2) in water, as a first step towards the elaboration of structured silica matrixes. A study in solution is first carried out in order to determine their amphiphilic behaviour, revealing that large planar objects are formed. Then the structural study of fresh materials obtained by a freeze drying process shows that different lamellar bilayer structures may form. Depending on the catalyst used during the sol-gel reaction, materials undergo very different structural evolutions with temperature. These results allow us to formulate a hypothesis on the lamellar assembling and the densification mechanism. Calculations of electronic densities cross-checked with thermal and ^{29}Si NMR analyses allow us to understand the mechanisms governing the lamellar stacking in each material. Finally we focus on the structural study at the interface between bilayers. The molecules and the general method are schematized in figure 1.

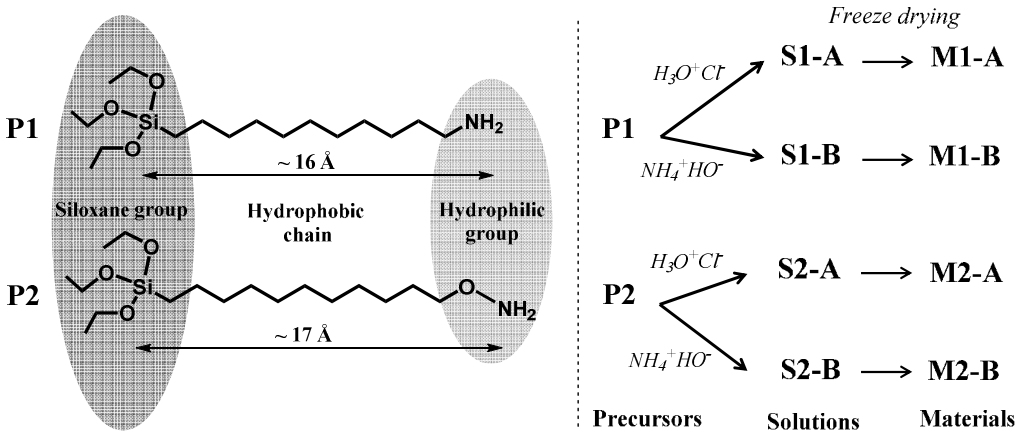

Figure 1. General description of organosilane "bola-amphiphile" precursor **P1** and **P2** (left) and the general procedure for the preparation of materials and their nomenclature (right).

Experimental

Technical details

Dynamic Light Scattering and Static Light Scattering (DLS/SLS) measurements were performed on an ALV-CGS3 with a red laser beam (λ=638.2nm) in a pseudo-cross correlation mode. The scattering angle was varied between 30° and 150° with steps of 2°. Temperature of the sample environment was controlled and stabilized at 20°C with an external thermostat. Sample tubes (5 mm round glass cells) were cleaned-up with ethanol in a home-build set-up and then dried. Experiments were performed with and without adding sodium chloride.

Raman spectra were recorded on a Horiba Jobin Yvon LabRAM Aramis confocal Raman microscope, using an excitation wavelength of λ = 532 nm with a laser spot size of ~1 µm and an objective of X50 long working distance. The incident laser power was kept lower than 0.8 mW in order to avoid any heating or structural sample damage. Scanning Electron Microscopy (SEM) was performed on FEI QUANTA 200 ESEM FEG operating at 15 kV equipped with a Everhart-Thornley detector.

Small Angle X-ray Scattering (SAXS) experiments were performed on a set-up operating in transmission geometry. A Mo anode associated to a Fox2D multi-shell mirror (XENOCS) delivers a collimated beam of wavelength 0.710 Å. Two sets of scatterless slits[25] delimitates the beam to a square section of side length 0.8 mm. A MAR345 imaging plate detector allows simultaneously recording scattering vectors q ranging from 0.25 nm^{-1} up to 25 nm^{-1}. Samples were placed in glass capillaries of 2 mm diameter. Absolute intensities were obtained by measuring a calibration sample of high density polyethylene (Goodfellow) for which the absolute scattering was already determined. All SAXS profiles are plotted in log-log scale in order to highlight the dependency of the intensity versus a power law of the scattering vector q.

Thermogravimetric Analyses (TGA) were performed on a Setaram Setsys Evolution 18 instrument under air flow (20 $mL.min^{-1}$) with a heating rate of 2 °$C.min^{-1}$. The coupled Mass spectrometer was a Hiden analytical QGA instrument.

Transmission Electron Microscopy (TEM) was performed on a JEOL 2200 FS operating at 200 kV. Samples obtained after heat treatment were ground into a powder and dispersed in ethanol. Samples were deposited on 400-mesh carbon-coated copper grids. After ethanol evaporation, the grid was submitted to analysis.

Precursor synthesis

Synthesis of P1.

The organic precursor P1 was synthesized in three steps in anhydrous conditions and according to a procedure adapted from the synthesis described in the literature[1,26]: bromoundecene (Alpha Aesar) was first mixed with triethoxysilane and Karstedt catalyst both purchased from ABCR to obtain bromoundecyl-triethoxysilane. After purification, the latter molecule was then used to form azidoundecyl-triethoxysilane with sodium azide (Sigma Aldrich) into acetonitrile. Reduction of the azido group with Palladium (10% Pd / C, Sigma Aldrich) into anhydrous ethanol under hydrogen atmosphere led to amino-undecyl-triethoxysilane.

Synthesis of P2.

The organic precursor P2 was synthesized in three steps as described in literature.[27] Bromoundecene (Alpha Aesar) was condensed with N-hydroxy-phtalimide in a Williamson's type reaction. Then a Gabriel's type reaction using hydrazine leads to amino-oxy-undecene. After purification, the latter molecule was mixed with triethoxysilane and Karstedt catalyst both

purchased from ABCR to obtain amino-oxy-undecyl-triethoxysilane.

All intermediate reactants and final products were purified by distillation under vacuum.

^{1}H, ^{13}C Nuclear Magnetic Resonance (NMR) and mass spectroscopy were used at each step in order to verify the structure and the purity of the different products; all the chemical characterizations were in agreement with the literature.[26,27]

Material syntheses

Samples were prepared as follows: 3 mmol of amino-undecyl-triethoxysilane (P1) or amino-oxy-undecyl-triethoxysilane (P2) were introduced in an acidic ($H_3O^+Cl^-$, CA = 6.16 10^{-2} mol.L-1) or a basic ($NH_4^+OH^-$, CB= 3.16 10^{-2} mol.L-1) aqueous solution (100 mL), respectively denoted A and B. Solutions S1-A and S1-B were prepared from the P1 precursor and S2-A and S2-B from the P2 precursor. In an attempt to compare the self-assembly and the condensation degrees as a function of the catalyst at the same concentration, and provided that the amino group is able to catch a proton (pKa = 9), the acid catalyst concentration was adjusted in such a way that it was equal to the one of ammonium hydroxide in B after formation of ammonium chloride groups.

Solutions S1-A, S1-B, S2-A, and S2-B have been stirred for ageing during three days foreword to be freeze-dried with a pressure of 0.8 torr for 3 days. Materials prepared in acidic conditions are named M1-A and M2-A. The ones prepared in basic conditions are named M1-B and M2-B. Then M1-A, M1-B and M2-A materials underwent a thermal treatment until 130°C for three days.

Results and discussion

Characterization of solutions

After addition of P1 and P2 in the aqueous solutions, the acidic solutions S1-A and S2-A remain clear while the ones prepared in basic condition S1-B and S2-B are cloudy and seem to have precipitated. The acidic solutions S1-A and S2-A have thus been investigated through DLS and SLS experiments in order to determine the size and shape of aggregates. SLS and DLS patterns are shown as supporting information in figures SI 1-4. The solutions have been diluted 50 times to meet the requirements of turbidity and viscosity for DLS measurement. The patterns expressing the mobility (Γ) and the reverse intensity (KC/R) as function of the squared scattering vector (q^2) do not exhibit straight lines. The SLS profiles suggest that Coulomb interactions occur[28] probably due to the ammonium moiety of the molecules. The DLS results ($\Gamma=f(q^2)$) give information on **the** hydrodynamic radius estimated at 250 nm while the SLS analyses ($KC/R = f(q^2)$) give a gyration radius of around 300 nm for both molecules. In order to screen the Coulomb interactions, sodium chloride salt has been added to the solutions according to the procedure related in the literature.[28-30] The DLS profiles are composed of two straight lines, each respectively indicating a hydrodynamic radius of 150 nm and 250 nm. The SLS pattern ($KC/R = f(q^2)$) then becomes a straight line. Therefore the apparent gyration radius could be evaluated to 500 nm. The SLS pattern $I/I0=f(q)$ shows a slope of q^{-2} which is characteristic of planar objects in the medium. Insofar as DLS theory assumes that aggregates are isotropic and monodisperse, the observed discrepancy between SLS and DLS measurements is not surprising, and the resulting size values must be handled carefully.

Structural study of fresh materials

After the sol-gel process, depending on the catalytic conditions used, different phenomena were observed. White solid foam-like materials (consisting of a network of interconnected structures that exhibits large amount of voids) were obtained from the acidic conditions (named M1-A and M2-A) while white fluffy powders were obtained under basic catalysis (named M1-B and M2-B). The SEM images of all samples suggest that the**ir** morphology at the micrometric scale consist**s** in thin stacked plates arranged in layers (Figure SI 5).

Information on the sample structure and on the progress of the sol−gel process can be obtained via Raman spectroscopy. Similar bands were observed for the different materials. The main bands located at 2845 cm^{-1} and 2880 cm^{-1} are attributed to the symmetric (s) and the antisymmetric (as) CH_2 stretching modes respectively (Figure 2a). The antisymmetric mode is clearly more intense than the symmetric one for all materials considering the peak heights. The peak height ratio I(as)/I(s) can be used to give information on the lateral order specifically on the hydrocarbon chain packing. Following the spectroscopic study dealing with a pure decylammonium chloride salt performed by Picquart *et. Al.,* a peak height ratio I(as)/I(s)=1.4 involve**s** a lamellar phase of alkylammonium chloride with molecules on a bidimensional hexagonal array.[31] In our case, a 1.3 – 1.4 ratio is observed**,** suggesting the presence of a lamellar structure in the materials.

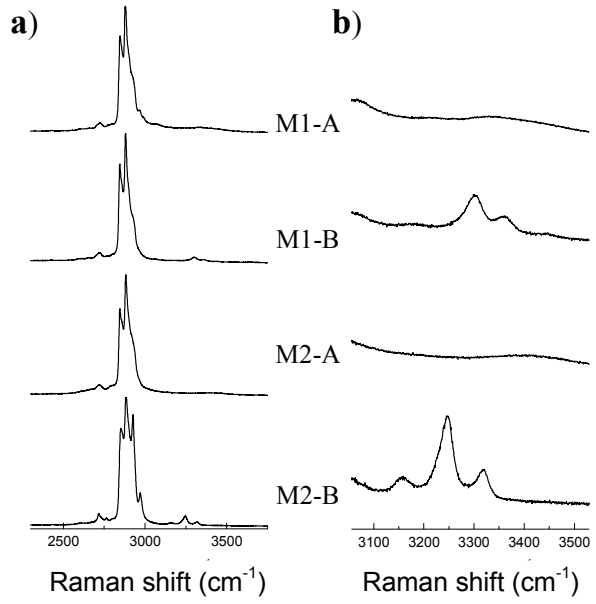

Figure 2. Raman spectra of materials M1-A, M1-B, M2-A and M2-B, focus between a) 2300 and 3750 cm^{-1} and b) 3050 and 3550 cm^{-1}.

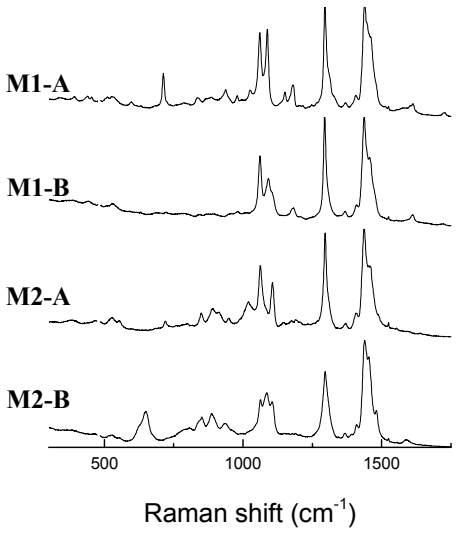

Figure 3. Raman spectra of materials M1-A, M1-B, M2-A and M2-B, focus between 300 and 1750 cm^{-1}.

The lamellar arrangement is also suggested by the C-C stretching vibration modes**.** One can observe an intense peak near 1060 cm^{-1} (Figure 3) due to the antisymmetric C-C vibrational modes in the trans-configuration**. T**he symmetric mode usually observable at 1120 cm^{-1} is missing. The bands corresponding to the stretching vibration mode**s** of gauche conformers are weak, or missing (845, 872 and 1080 cm^{-1})**,** meaning that the aliphatic chains are predominantly in all trans-conformation.[31] Such a conformation implies that the chain is fully extended, promoting the formation of a lamellar arrangement.

The spectra also show discrepancies linked to their different terminal polar head group, namely the amino or the amino-oxy groups. The peaks between 1090 and 1110 cm^{-1} in figure 3 could be attributed to the C-N or C-O stretching vibration modes for M1 and M2 type materials, respectively. The spectra of M1-B and M2-B are also respectively characterized by two and three bands at 3100-3400 cm^{-1} corresponding to the N-H stretching vibration modes (Figure 2b). The M1-A and M2-A materials do not exhibit such bands, involving that the stretching mode is not allowed, which is probably due to the presence of ammonium chloride species.

In figure 3, the Si-O-Si vibration modes[32,33] at 450 and 530 cm^{-1} present a low intensity, which is easily understandable taking into consideration the weak amount of silica fraction inside the materials. The Si-OH stretching modes at 930-1020 cm^{-1} are of higher intensity in the spectra of the M1-A and M2-A materials, suggesting a weaker condensation ratio than in the materials made in basic conditions. The band respectively appearing at 713 and 718 cm^{-1} on the spectrum of the M1-A and M2-A materials is due to the presence of free trisilanol groups of totally hydrolyzed compounds adsorbed on the material.

Finally the spectrum of the M2-B sample is the only one showing two bands at 630 and 650 cm^{-1} featuring the stretching vibration modes (symmetric and antisymmetric) of totally unhydrolyzed triethoxysilane molecules.[34] This observation involves a weak hydrolysis ratio.

In order to confirm the results suggested by Raman spectroscopy concerning the hydrolysis and condensation ratio of the siloxane parts inside the materials, ^{29}Si solid state NMR experiments have been performed. The percentage of the different T^x substructures in the materials obtained by the deconvolution of the spectra (Figure SI 6) are reported in Table 1.

Table 1: ^{29}Si solid state NMR analysis results for samples M1-A, M2-A and M1-B, M2-B.

T^x	M1-A	M1-B	M2-A	M2-B
T^0	7	0	4	29
T^1	14	8	8	2
T^2	67	38	59	31
T^3	12	54	29	39

^{29}Si solid state NMR clearly indicates that the Si-C bond is retained during the sol-gel reaction since only T^x units are resolved. No resonance attributable to SiO_2 groups (Q units) is observed. The results for M1-A and M2-A materials are similar with a major

substructure T^2 ($CSi(OSi)_2OH$) and minor substructures of T^0 $CSi(OX)_3$ (X=OEt, H), T^1 $CSi(OSi)(OH)_2$ and T^3 $CSi(OSi)_3$. This indicates that the materials are moderately condensed. The M1-B material presents a higher condensation ratio with predominant T^3 and T^2 units, in good agreement with the usual observations in basic conditions. This is also the case for the M2-B material which shows the presence of a narrow peak at -47 ppm, corresponding to T^0 units. Interestingly, the presence of a amino-oxy or a amine group could affect the hydrolysis-condensation rate in regards to the basic condition.

The meso-structure of materials resulting from the self-assembly of precursors (P1) and (P2) were investigated by SAXS. Figure 4 displays the SAXS patterns obtained for the four fresh materials after the freeze-drying process.
Focusing on the small angle part of diagrams, the intensity follows a q^{-4} power law. Such a power law is known as a Porod law and is typical of sharp interfaces between the aggregates and the surrounding medium for a typical length scale larger than 10 nm.

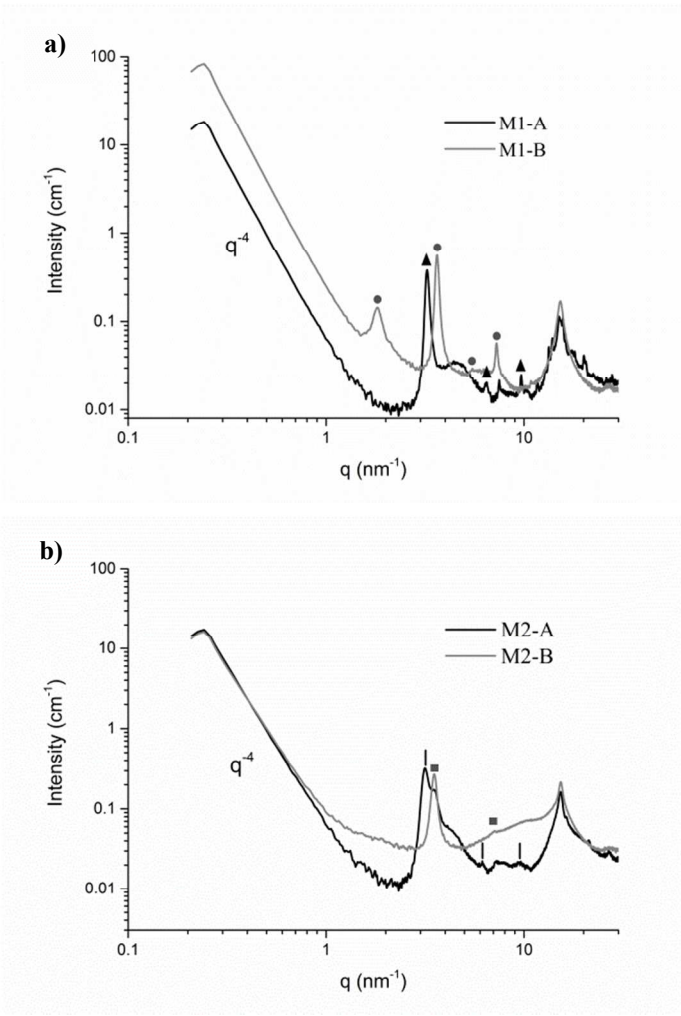

Figure 4. SAXS profiles of material M1 (a) and M2 (b).

The largest feature observable around 15 nm^{-1} (typical distance of 0.42 nm in the real space) can be related to the typical mean lateral distance between two precursors.[24] A large shoulder ranging from 6 to 9 nm^{-1} is observable in the diagram of M2-B and is not visible in the others. The latter feature can be attributed to the mean distance between two silicon groups linked by 2 ethoxy groups, as in 2 neighbouring molecules which is in agreement with the Raman and ^{29}Si NMR results for the M1-B material. Recently, we described by means of *in situ* SAXS experiments the disappearing of the same shoulder when the poly-condensation occurs.[24]
Four structure peaks are clearly identified on the M1-B SAXS profile and are highlighted by disks in figure 4. These peaks, for which the q_n/q_1 ratio is an integer n (Table 2), are characteristic of a lamellar structure as proposed by Raman spectroscopy results.

Table 2. q values of structure peak appearing in the SAXS pattern of materials M1-A, M1-B, M2-A and M2-B. Peaks are qualified as weak (w), doubled (d), broad (b). The lattice parameter (a) of the associated lamellar structure is also given.

Samples	Symbols	q_1	q_2	q_3	q_4	a
M1-A	▲	3.2	6.4	9.6		19.6
M1-B	●	1.8	3.6	5.4(w)	7.2	34.9
M2-A	▬	3.1/3.5(d)	6.2/7.0(d)	9.3 (b)		20.3
M2-B	■	3.5	7(w)	-		17.9

A lamellar structure could be given by the stacking of monolayers (hypothesis H_α) or bilayers (hypothesis H_β), as described in figure 5.
The lattice parameters deduced from the analysis of peak positions are indexed in Table 2. In H_α, monolayers are made by a condensed silica plane decorated with P1 or P2 molecules on one side. In H_β, bilayers are made by a central silica plane decorated with P1 or P2 molecules on its both sides. The stacking of these larger objects results in an increased lattice parameter of the lamellar structure. Here, the first structure peak appears at q1 = 1.8 nm-1, meaning that the electronic density of the silica matrix ρs is periodically repeated each 3.5 nm.

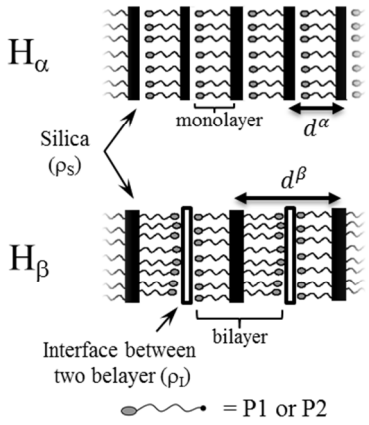

Figure 5. Hypotheses (H_α and H_β) proposed for the structure of materials.

This value corresponds to the hypothesis of a bilayer lamellar structure (H_β). This observation is in agreement with the works of Alauzun *et al.*[23], albeit involving a larger lattice parameter. One can remark that the odd order Bragg features appear wider and less intense than the even order features.

The SAXS pattern of M1-A and M2-A exhibits some peaks from 3.2 nm^{-1} to 27 nm^{-1} and a large lump located around 4 to 4.5 nm^{-1}. The materials seem to present several phases, but one of them can be determined for each material. Indeed, the ratio $q_n/q_1 = n$ is respected by the peaks located at $q_1 = 3.2$ nm^{-1}, $q_2 = 6.4$ nm^{-1}, and $q_3 = 9.6$ nm^{-1} for M1-A and $q_1 = 3.1$-3.5 nm^{-1}, $q_2 = 6.2$-7.1 nm^{-1} and $q_3 = 9.5$ nm^{-1} for sample M2-A. These sets of peaks correspond to lamellar structures. However, other peaks are visible in the SAXS pattern of M1-A and M2-A and could not be easily indexed. In the M1-B and M2-B SAXS pattern, no other peak than those related to the lamellar structure is observed. Thus, the additional peaks in the SAXS pattern of M1-A and M2-A might be due to the formation of another crystalline structure, specific of the acidic catalysis. The lattice parameter of the lamellar structures is estimated at around 1.9-2.0 nm, which is quite smaller than the expected lattice-parameter for the bilayer structure. Two hypotheses might be considered in order to describe this result. On one hand, it could be related to the formation of monolayers presenting a lattice parameter d^α (hypothesis H_α in figure 5). On the other hand, it could be related to bilayers of lattice parameter d^β where the silica planes and the interfaces between bilayers have the same electron density (hypothesis H_β in figure 5). As a matter of facts, such a configuration would result in the extinction of the Bragg peaks of odd indexes.

In acidic conditions, the fast hydrolysis and the formation of ammonium chloride groups instead of amino groups improve the amphiphilic behaviour of the molecules. They are more easily solvated and they condensate progressively, leading to the formation of large planar objects in solution. By freeze-drying the solution, the planar objects collapse and stack randomly on top of each other leading to lamellar foam-like materials.

In contrast, in basic conditions, the solution becomes quickly turbid due to the fact that the amino part is not enough hydrophilic to lead to a homogeneous solution. The amphiphilic molecules are almost not solubilized and stay inside droplets. They self-organize in lamellar structure as the condensation occurs, leading to small aggregates.

Structural evolution of materials with temperature

In order to stabilize the materials and determine their final structure, we followed the structural changes during a thermal treatment by performing an *in situ* temperature SAXS experiment. Starting from freeze-dried powders, the temperature was raised from 20°C up to 130°C.

In situ SAXS measurements (Figure 6) exhibit important structural modifications for all samples.

Globally, the structure of heated materials prepared with acidic conditions seems to be better defined than that of fresh materials, as can be deduced from the decrease of the Bragg peak width. On the contrary, the structure of the M1-B material seems to be damaged under heating.

In the first part of the heating process, *i.e.* until 80°C, the M1-B lamellar structure is slightly contracted as indicated by the shift of structure peaks toward the larger q values. From 100°C the lamellar structure starts to disappear and an amorphous structure is observed beyond 120°C.

The structure of the M2-B material is also first slightly contracted. From 60°C, two supplemental peaks progressively appear at 2.15 nm^{-1} and 6.4 nm^{-1} and their intensity increases untill 120°C. The large shoulder ranging from 6 to 9 nm^{-1} is still observable in the diagram, revealing that the hydrolysis of ethoxysilane groups is far to be complete, even after an annealing at 130°C for 3 days. After cooling the structure does not remain and seems to be amorphized. Consequently, no supplementary study was led on this sample.

The SAXS patterns of M1-A and M2-A show a broadening and a strong intensity decrease of structure peaks at highest angles between 60°C to 80°C, followed by that of the lump – initially located at around 4-4.5 nm^{-1} – between 80°C to 100°C.

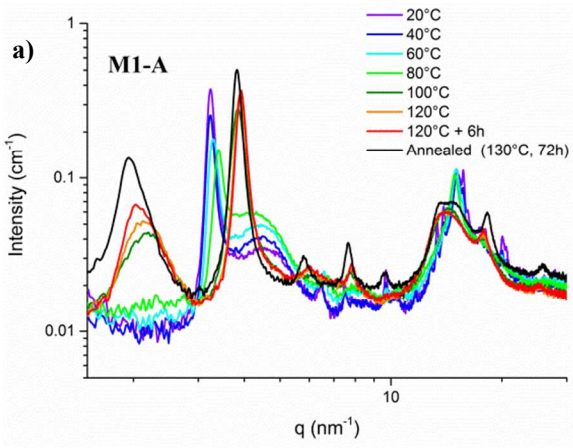

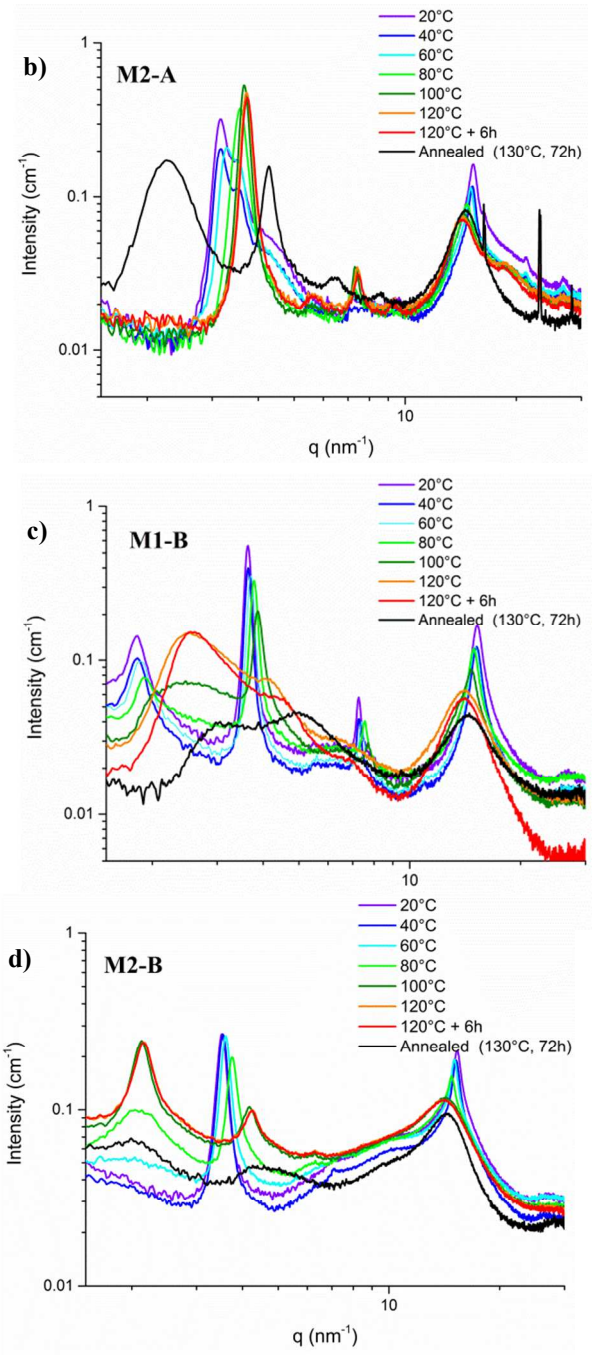

Figure 6. In situ temperature SAXS experiment from 20°C (fresh samples) to 120°C : a) M1-A, b) M2-A c) M1-B and d) M2-B. Sample temperature has been stabilized for 6 hours between each measurement. The black SAXS profile concerns samples annealed at 130°C for 72h and measured at 20°C.

Simultaneously, in the same range of temperature, two features located at 2.2 nm^{-1} and 6.6 nm^{-1} appear on the M1-A SAXS profile. These peaks downshift at higher temperature to 1.95 nm^{-1} and 5.9 nm^{-1}, respectively. In the same time, the 5th order of scattering of the lamellar structure appears at 10 nm^{-1}, and the peak initially located at 3.2 nm^{-1} shifts to 3.9 nm^{-1}. The same phenomenon is observed on the M2-A SAXS patterns, but the latter peak appears after an annealing at 130°C for 3 days.

The second hypothesis (H_{ϖ} in figure 5) is compatible with such observations. In the SAXS pattern of a lamellar structure, the intensity of the Bragg peaks depends on the electronic contrast between stacked layers. If we assume that the silica planes and the interfaces between bilayers (see figure 5) have the same electron density in M1-A and M2-A, then the characteristic distance from the electronic density point of view will be half of the d_{β} distance. Bragg peaks will accordingly appear at the positions expected for a lamellar lattice in which the characteristic distance is equal to half of the distance between silica planes. Upon heating, the electronic density of the silica plane increases. The electronic contrast between silica plane and the interface between bilayers thus becomes different. As the lattice parameter is doubled because it becomes equal to the distance between silica planes, new peaks appear and correspond to the odd orders of the lamellar structure. We assume that the change of electronic density during the heating could be associated to the densification of the silica matrix. Indeed, during the sol-gel process, the siloxane part of precursors first undergoes a hydrolysis step of the ethoxy group leading to silanol ($R\text{-}Si(OEt)_{3-n}(OH)_n$, $0 \leq n \leq 3$). Then the poly-condensation reaction allows to form the silica matrix by making oxygen bridges ($R\text{-}SiO_{(1.5-n/2)}(OH)_n$). Note that we will further refer to the polycondensation state of the organosilane precursor by using the usual notation T^{3-n}.

In order to confirm the validity of hypothesis H_{β}, the electronic density of each part of the stacked structure was calculated and the results were cross-checked with results of thermal measurements and ^{29}Si NMR analyses.

Densification mechanism (simulation and thermal analysis)

The electronic density of the silica matrix and that of the interface between bilayers (possibly an ammonium chloride phase for M1-A material) can be calculated from the electron numbers and the molar volumes listed in table 3. Those of oxygen, hydroxide group and amine fragment have been estimated thanks to Fedors' table.[35]

Table 3. Number of electrons and molar volume of the different chemical groups found in the materials.

	Si	O	OH	$-NH_2$	HCl	H_2O	CO_2
i	1	2	3	4	5	6	7
Electron number	14	8	9	10	18	10	22
Molar volume ($cm^3.mol^{-1}$)	19.7	3.8	13	19	15	18	18

The value for silicon has been deduced from a density close to 2.23, and the molar volume of the chloride ion has been calculated from its ionic radius. The molar volume of ammonium chloride is the same that the expected value for a pure crystalline ammonium chloride phase (*i.e.* μ=1.53 $g.cm^{-3}$).

The electronic density of silica has been calculated based on the formula -Si-$O_{(1.5-n/2)}(OH)_n$ for the silica matrix where n corresponds to the number of hydroxyl groups per silicon atom ($0 \leq n \leq 3$). The interface is constituted by the ammonium chloride phase where hydrochloric acid and water can vary with x and y as -NH_2• HCl_{1+x}, H_2O_{x+y}. The electronic density noted ρ is usually expressed in $e^-.cm^{-3}$. Here we choose to keep the electronic density in $mol.cm^{-3}$ for simplicity. This parameter can be easily calculated from the expression:

$$\rho_i = \frac{e_i}{v_i}$$

$$\rho = \frac{\sum_i \alpha_i e_i}{\sum_i \alpha_i v_i}$$

where α_i, e_i and v_i are respectively the number, the electron number and the molar volume of the fragment i (see what i refers to in Table 2). We first focus on the case of the M1-A material. **T**he electronic density at the interface of bilayers can be estimated by the following expression:

$$\rho_I^{M1-A}(x,y) = \frac{e_4 + e_5(1+x) + e_6(x+y)}{v_4 + v_5(1+x) + v_6(x+y)}$$

In order to determine the electronic density upper limit at the interface of bilayers, we can minimize y and maximize x, *i.e.* we consider only $H_3O^+Cl^-$ at the interface.

$$\lim_{x\to\infty} \rho_I^{M1-A}(x,0) = \frac{e_4 + e_5(1+x) + xe_6}{v_4 + v_5(1+x) + xv_6}$$

$$\lim_{x\to\infty} \rho_I^{M1-A}(x,0) = \frac{e_5 + e_6}{v_5 + v_6}$$

In order to determine the smallest value of the electronic density at the interface of bilayers, we can minimize x and maximize y. This operation aims at considering only water at the interface.

$$\lim_{y\to\infty} \rho_I^{M1-A}(0,y) = \frac{e_4 + e_5 + ye_6}{v_4 + v_5 + yv_6}$$

$$\lim_{y\to\infty} \rho_I^{M1-A}(0,y) = \frac{e_6}{v_6}$$

Thus the electronic density can be bounded as follows.

$$\lim_{y\to\infty} \rho_I^{M1-A}(0,y) < \rho_I^{M1-A}(x,y) < \lim_{x\to\infty} \rho_I^{M1-A}(x,0)$$

$$\frac{5}{9} < \rho_I^{M1-A}(x,y) < \frac{28}{33}$$

This approach allowed us to bound the electronic density of the interface between bilayers. Let us now consider how the electron density evolves in the silica planes.

The thermal analysis of M1-A under air flow (see figure 7a-b) exhibits successive losses of water (5-6 wt. % of the initial material) associated with an endothermic reaction (between 40°C and 110°C). It could occur when poly-condensation starts in relation with the disappearing of T^0 compounds between 40°C and 75°C. The condensation of T^0 compounds leads to the formation of oxygen bridges at the extremity of the established network. This phenomenon is not expected to affect the structure, which is in good agreement with the SAXS results. It can be noticed that no shift on the structure peak located at 3.2 nm^{-1} is observed during this first phase (Figure 7c). However its intensity decreases. This suggests that the contrast between the silica matrix and the interface between bilayers decreases. The densification therefore occurs without any modification of the structure. The second water loss between 75°C and 110°C is probably due to the release of water while T^1 silicon (…-$SiO_{½}(OH)_2$) transforms into T^2 (…-$SiO_1(OH)$).

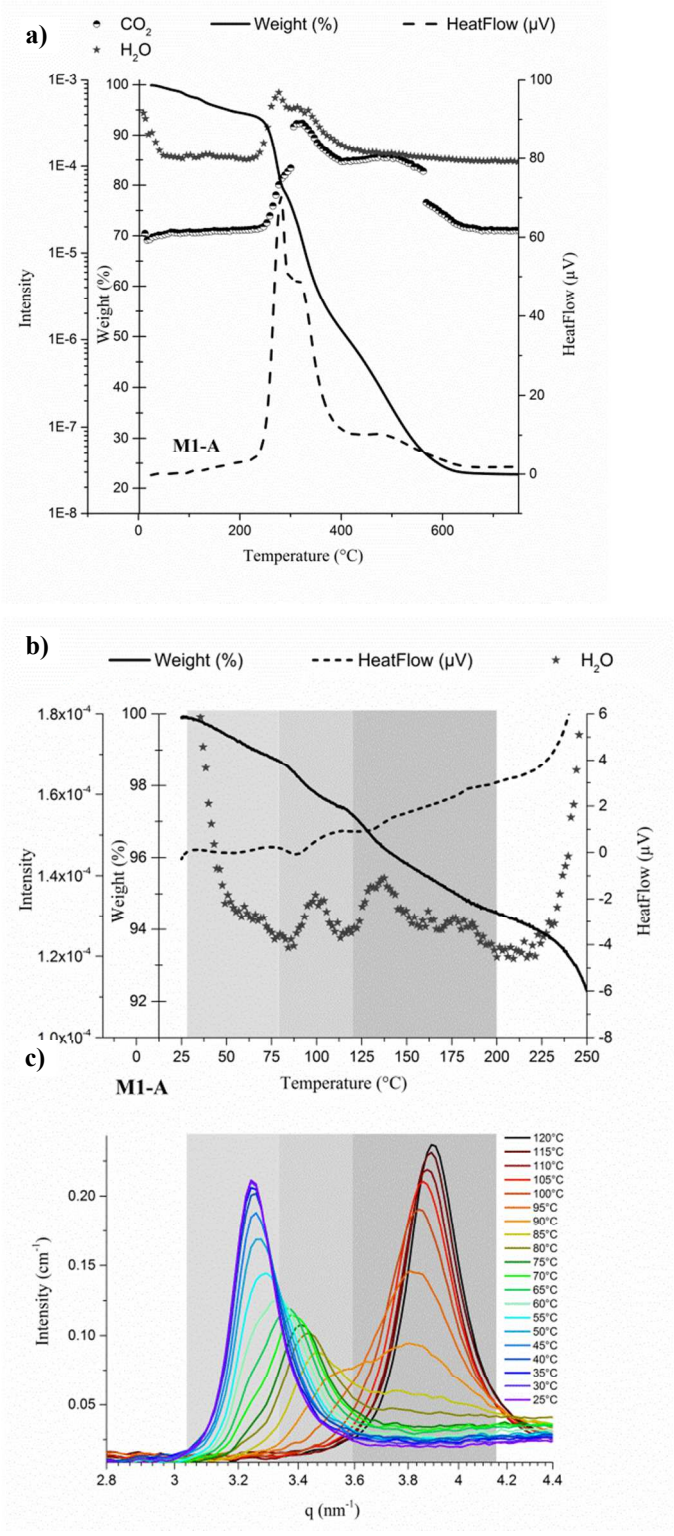

Figure 7. a) Complete thermal analysis of sample M1-A involving weight losses, heatflow, and gas released. b) A focus closely on the region between 25°C and 250°C of the TGA. c) *In situ* temperature

SAXS experiment focused on the [3 - 4.4 nm^{-1}] q range, with temperature steps of 5°C. Background colours ranging from lighter to darker grey respectively refer to the disappearance of T^0, T^1 and T^2 compounds.

This phenomenon takes place inside the network, whose structure is consequently affected. It is indeed simultaneously observed on the SAXS pattern through the disappearance of the lump at 4-4.5 nm^{-1} and the shift of the structure peak initially located at 3.2 nm^{-1} to 3.8 nm^{-1}. At this level, the electronic density of the silica matrix is large enough compared to that of the interface between two bilayers to make odd peaks appear, as discussed in the previous paragraph. The third loss occurs between 110°C and 170°C which could be due to the departure of water during the conversion of T^2 compounds into T^3 compounds. The *in situ* SAXS profiles shown in figure 7c depict in more detail the simultaneous disappearance of the Bragg peak related to the low temperature structure and the appearance of that related to the condensed structure. The solid state NMR ^{29}Si analysis of M1-A after the thermal treatment at 130°C gives 61% of T^3 and 39% of T^2 and shows the complete elimination of T^1 and T^0, evidencing the densification of the silica matrix (see figure SI 8).

Thanks to the latter solid state ^{29}Si NMR results and thermal analysis, it has been possible to calculate the electronic density of the fragment $-SiO_{(1.5-n/2)}(OH)_n$ for different temperatures.

$$\rho_S^{M1-A}(n) = \frac{e_1 + e_2(1.5 - 0.5n) + ne_3}{v_1 + v_2(1.5 - 0.5n) + nv_3}$$

The figure 8a shows the calculated ρ_S^{M1-A} versus n, and the smallest value of relative electronic contrast $\Delta\rho_{min}$ between the silica layer and the ammonium chloride layer versus n. $\Delta\rho_{min}$ is minimized by the electronic density upper limit at the interface of the bilayers, i.e. considering only $H_3O^+Cl^-$ at the interface. Its expression is thus:

$$\Delta\rho_{min} = \rho_S^{M1-A}(n) - \lim_{x\to\infty} \rho_I^{M1-A}(x,0)$$

According to the thermal analysis (see figure 7a-b), the disappearance of hydroxyl groups bounded to silicon atoms can be related to the temperature. This phenomenon leads to the densification of the silica matrix with temperature, as schematized on figure 8b. Therefore, the increase of electronic density of the silica layer with the temperature leads to an increase of $\Delta\rho_{min}$. It confirms the scenario described in the latter paragraph and allows us to exlain the peculiar evolution we observed during in situ SAXS experiments.

The same trend is seen in the M2-A material, but the electronic density of the interface of bilayers is expected to be higher because of the supplementary oxygen contained in the amino-oxy function of P2 in the fragment $-ONH_2{\bullet}HCl_{1+x},H_2O_{x+y}$. The electronic density of such a fragment is expressed as described below.

$$\rho_I^{M2-A}(x,y) = \frac{e_2 + e_4 + e_5(1+x) + e_6(x+y)}{v_2 + v_4 + v_5(1+x) + v_6(x+y)}$$

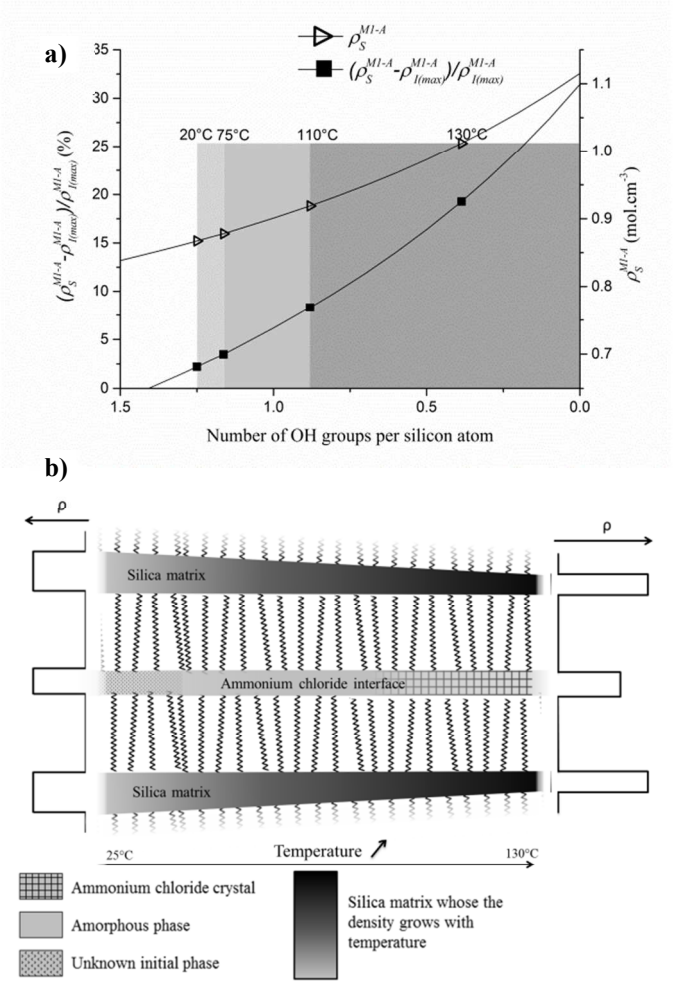

Figure 8. a) Electronic contrast between the silica walls and the ammonium chloride interface (left scale) and electronic density of silica walls (right scale) for M1-A material as function of number of silanol groups. b) Schematic representation of the densification phenomenon.

It can be bound following a procedure similar to the case of M1-A described above. The $\rho_I^{M2-A}(0,0)$ given by the fragment $-ONH_2{\bullet}HCl$ is the highest calculated value which corresponds to the final fragment obtained at 130°C.

$$\lim_{y\to\infty} \rho_I^{M2-A}(0,y) < \rho_I^{M2-A}(x,y) < \rho_I^{M2-A}(0,0)$$

$$\frac{5}{9} < \rho_I^{M2-A}(x,y) < \frac{20}{21}$$

Accordingly, the electronic contrast between ρ_I and ρ_S becomes important at higher densification ratio than for M1-A. For instance, at 130°C, it can be calculated that the electronic contrast reaches 9% between silica matrix and interface.

We finally focus on the case of the M1-B material. The NMR resonance signals obtained for M1-B (see Table 1) show that the condensation of the silica matrix is initially more important than for M1-A or M2-A. In comparison the M1-B fresh material has a similar densification ratio than annealed M1-A, thus the losses observed by thermal analysis until 110°C (see

figure 9) are due to the CO_2 and physisorbed water (4.7 wt.% including 1.2% of pure water and 3.5% of H_2CO_3).

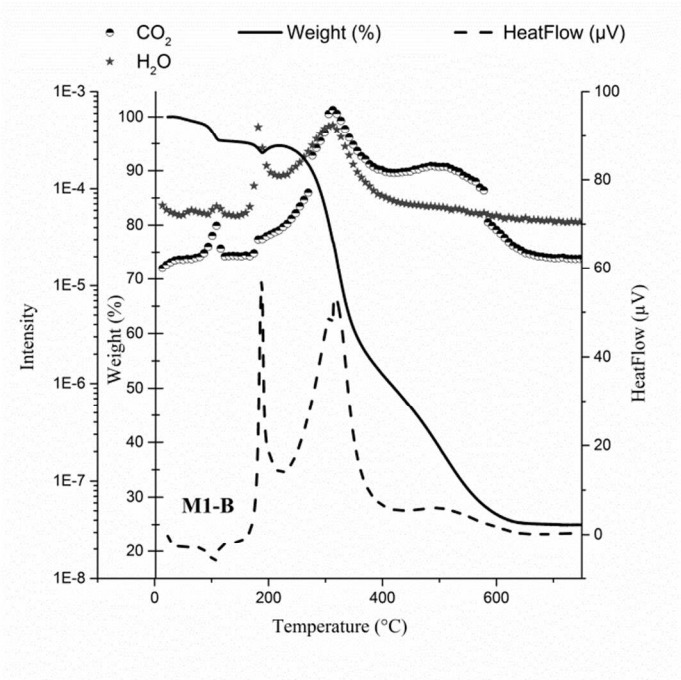

Figure 9. Thermal analysis of M1-B.

The residual mass (24.9 w. %) after calcination can be considered as that of pure silica of molar mass 60 g.mol^{-1}. It has therefore been possible to determine the exact composition as $(OH)_{0.54}O_{1.23}Si$-$(CH_2)_{11}$-NH_2, 0.15 CO_2, 0.30 H_2O. The deduced electronic density of the interface was evaluated to 0.59 mol.cm^{-3} and the electronic contrast between silica walls and interface was evaluated to 65%.

The structural study and the electron density calculations allowed us to precise the mechanism of densification of the materials under thermal treatment. Although the SAXS profiles of fresh materials can be different as function of catalyst, the molecular organization remains similar.

Study of the interfaces between bilayers (structure and composition)

In order to get insights into the mechanisms governing the lamellar stacking of P1 and P2 molecules, we focus on the SAXS profiles of the annealed M1-A and M2-A materials at higher q values (see figure 6). After annealing**,** an unexpected observation can be noted. Although the P2 molecule is larger than the P1 molecule, the annealed M1-A material (noted M1-Aa) presents a larger lattice parameter than the annealed M2-A material (noted M2-Aa), as indexed in Table 4.

Table 4. q values (nm^{-1}) of the structure peaks characteristic of a lamellar lattice as a function of annealed materials, and the corresponding lattice parameter a_1 values (nm).

Samples	q_1	q_2	q_3	q_4	q_5	a_1
M1-Aa	1.96	3.8	5.8	7.7	9.7	**3.2**
M1-Ba	3(br)	5(br)	-	-	-	
M2-Aa	2.2	4.2	6.5	8.5	-	**2.9**

Furthermore, both of them present three structure peaks at wide angles. M1-Aa shows three broad peaks located at 13.6 nm^{-1}, 18.3 nm^{-1} and 25.8 nm^{-1}, and in M2-Aa some peaks appear doubled but intense at 16.3 nm^{-1}, 23 nm^{-1} and 28.1 nm^{-1}. These peaks seem to correspond to Bragg reflections on the planes (100), (110) and (111) of a simple cubic structure of lattice parameter a=4.7 Å for the M1-Aa sample and a=3.85 Å for the M2-Aa sample. Both samples have been prepared with hydrochloric acid (pH=1.5) as catalyst, implying that the amino group is under ammonium form. Only chloride ions have been introduced in the medium as anions. The EDX analysis shows that chlorine remained in the material after freeze-drying. The SAXS profiles of samples prepared from basic conditions (M1-B and M2-B) do not present similar peaks when increasing temperature. No chlorine has been either detected in the materials by EDX measurement. Therefore, the observed additional peaks in SAXS profile of M1-A and M2-A could be due to mono-substituted ammonium chloride phase. The M2-A structure peaks are close to those expected for an ammonium chloride cubic structure (q_{100}=16.3 nm^{-1}, q_{110}=22.8 nm^{-1}, q_{111}=28.2 nm^{-1}).[36]

The planes (110) at the surface of lamellar aggregates are visible in TEM images (see figure 10). The lamellar structure of M1-Aa and M2-Aa materials seems to be improved as the intra-lamellar structure is formed. The interactions at the interfaces are thus an important parameter in the comprehension of the cohesion of the structure.

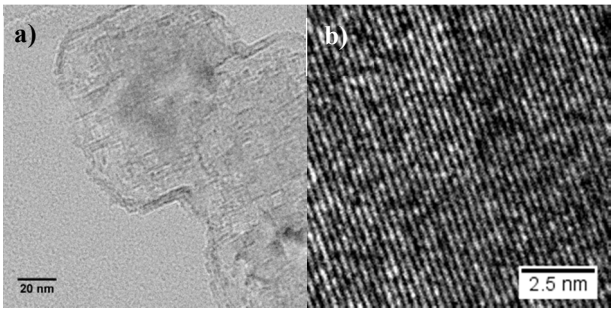

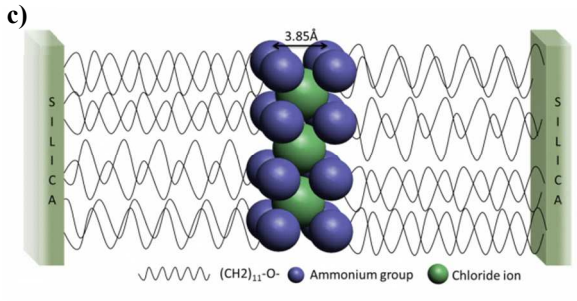

Figure 10. TEM images: (a) M2-A material exhibiting lamellar structures and (b) the (110) planes of an ammonium chloride cubic structure. (c) Schematic representation of the intra-lamellar structure.

Carbon dioxide is described in previous works as an assembly agent[20,21] and could govern the mesostructure.

As shown in Figure 9, thermal measurements of the M1-B sample exhibit a phase transition between 86°C and 105°C associated with a departure of CO_2 and water measured with mass spectroscopy. *In situ* temperature SAXS patterns of M1-B show a phase transition at around 80°C (see Figure 6). The features initially located at 1.8 nm^{-1} shifts until 80°C and become a broad lump after 100°C. An amorphization of M1-B seems to occur then. The CO_2 release mechanism is schematized in Figure 11. The carbon dioxide adsorbed on amine functions would therefore appear as both an assembly and cohesion agent of the lamellar structure in M1-B material. Ammonium chloride species play the same role in M1-A and M2-A samples but the structure is immobilized.

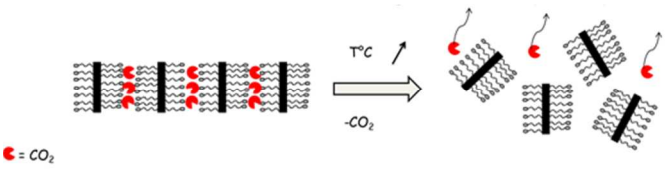

Figure 11. Schematic representation showing CO2 as cohesion agent released with thermal treatment.

Conclusions

The self-assembly behaviour of amino-undecyl-triethoxysilane (P1) and amino-oxy-undecyl-triethoxysilane (P2), which can be considered as "bola-amphiphiles" were studied in water in acidic or basic catalytic conditions. The study does not show critical discrepancy between the self-assembly of both precursors, except for the crystallization of the ammonium chloride phase at the interface.

Acidic solutions S1-A and S2-A by DLS and SLS measurements confirm the formation of large planar objects in the firsts hours of ageing. The freeze drying process on those solutions led to white foams composed of interconnected layered aggregates. Those prepared in basic conditions provided layered pulverulent powders. Although fresh materials exhibit different SAXS pattern, the study demonstrated that in any catalytic condition, the aggregation process led to a lamellar structure. Nevertheless, significant differences in terms of hydrolysis and condensation were shown. In acidic condition, we reported a reduced condensation ratio compared to the basic condition. Among the tested compositions, we focused on M1-A materials, on which we could describe the multistep mechanism of densification of silica matrix using *in situ* temperature SAXS experiments coupled with calculations of electronic density, solid state NMR, and thermal analysis.

The unexpected appearance of the ammonium chloride type structure on M1-A and M2-A material and the phase transition observed on M1-B during heating, revealed that the structure is maintained by the presence of cohesion agents. Thus the silica matrix does not seem to be the main parameter that governs the self-assembly in the system.

Acknowledgements

The authors acknowledge C. Rey for her help on thermal analysis aspects, R. Turgis for assistance on organic synthesis and on characterization of organic compounds, X. Le Goff for his help on TEM measurements and assistance in the image processing, and S. Maynadié for support in solid state NMR analysis.

Notes and references

Institut de Chimie Séparative de Marcoule, UMR 5257 CEA/CNRS/UM/ENSCM, BP17171, F-30207 Bagnols-sur-Cèze, France.
E-mail: guilhem.arrachart@cea.fr ; julien.cambedouzou@enscm.fr

Electronic Supplementary Information (ESI) available: DSL/SLS measurements of acidic solutions S1-A and S2-A (Figure SI 1-4); SEM images of the materials (Figure SI 5); ^{29}Si solid-state NMR of the materials (Figure SI 6).

See DOI: 10.1039/b000000x/

1 S. Lambert, K. Y. Tran, G. Arrachart, F. Noville, C. Henrist, C. Bied, J. J. E. Moreau, M. Wong Chi Man, B. Heinrichs, *Microporous Mesoporous Mater.*, 2008, **115**, 609–617.
2 D. Trong On, D. Desplantier-Giscard, C. Danumah, S. Kaliaguine, *Appl. Catal. Gen.*, 2001, **222**, 299–357.
3 W. Otani, K. Kinbara, Q. Zhang, K. Ariga, T. Aida, *Chem. – Eur. J.*, 2007, **13**, 1731–1736.
4 X. Feng, G. E. Fryxell, L.-Q. Wang, A. Y. Kim, J. Liu, K. M. Kemner, *Science*, 1997, **276**, 923–926.
5 S. Bourg, J.-C. Broudic, O. Conocar, J. J. E. Moreau, D. Meyer, M. Wong Chi Man, *Chem. Mater.*, 2001, **13**, 491–499.
6 G. Arrachart, I. Karatchevtseva, D. J. Cassidy, G. Triani, J. R. Bartlett, M. Wong Chi Man, *J Mater Chem.*, 2008, **18**, 3643–3649.
7 R. Turgis, G. Arrachart, C. Delchet, C. Rey, Y. Barré, S. Pellet-Rostaing, Y. Guari, J. Larionova, A. Grandjean, *Chem. Mater.*, 2013, **25**, 4447–4453.
8 L.-Y. Yuan, Y.-L. Liu, W.-Q. Shi, Z. Li, J.-H. Lan, Y.-X. Feng, Y.-L. Zhao, Y.-L. Yuan, Z.-F. Chai, *J. Mater. Chem.*, 2012, **22**, 17019–17026.
9 H. Oviatt, K. Shea, S. Kalluri, Y. Shi, W. Steier, L. Dalton, *Chem. Mater.*, 1995, **7**, 493–498.
10 G. H. Hsiue, R. H. Lee, R. J. A. Jeng,. *Chem. Mater.*, 1997, **9**, 883–888.
11 B. Lebeau, S. Brasselet, J. Zyss, C. Sanchez, *Chem. Mater.*, 1997, **9**, 1012–1020.

12 Z. Chen, L. Samuelson, J. Akkara, D. Kaplan, H. Gao, J. Kumar, K. Marx, S.Tripathy, *Chem. Mater.*, 1995, **7**, 1779–1783.
13 J. Livage, *C. R. Acad. Sci.*, 1996, **322**, 417–427.
14 D. Tian, P. Dubois, C. Grandfils, R. Jerome, P. Viville, R. Lazzaroni, J. L. Bredas, P. Leprince, *Chem. Mater.*, 1997, **9**, 871–874.
15 A. Charlot, S. El Mourabit, F. Goettmann, G. Arrachart, R. Turgis, A. Grandjean, *RSC Adv.*, 2014, 64138–64141.
16 (a) A. Walcarius, L. Mercier, *J. Mater. Chem.*, 2010, **20**, 4478–4511 ; (b) H. Yoshitake, *J. Mater. Chem.*, 2010, **20**, 4537–4550.
17 F. Hoffmann, M. Cornelius, J. Morell, M. Froba, *Angew. Chem. Int. Ed.*, 2006, **45**, 3216 – 3251.
18 (a) G. Arrachart, G. Creff, H. Wadepohl, C. Blanc, C. Bonhomme, F. Babonneau, B. Alonso, J.-L. Bantignies, C. Carcel, J.J. E. Moreau, P. Dieudonné, J.-L., Sauvajol, D. Massiot, M. Wong Chi Man, *Chem. Eur. J.*, 2009, 15, 5002 – 5005 ; (b) G. Arrachart, C. Carcel, P. Trens, J.J. E. Moreau, M. Wong Chi Man, *Chem. Eur. J.*, 2009, **15**, 6279 – 6288; (c) G. Arrachart, A. Bendjerriou, C. Carcel, J. J. E. Moreau, M. Wong Chi Man, *New J. Chem.*, 2010, **34**, 1436–1440.
19 E. Ruiz-Hitzky, S. Letaïef, V. Prévot, *Adv. Mater.*, 2002, **14**, 439–443.
20 Q. Zhang, K. Ariga, A. Okabe, T. Aida, *J. Am. Chem. Soc.*, 2004, **126**, 988–989.
21 R. Voss, A. Thomas, M. Antonietti, G. A. Ozin, *J. Mater. Chem.*, 2005, 4010–4014.
22 K. Katagiri, M. Hashizume, K. Ariga, T. Terashima, J. Kikuchi, *Chem. Eur. J.*, 2007, **13**, 5272 – 5281.
23 (a) J. Alauzun, A. Mehdi, C. Reye, R. J. P. Corriu, *J. Am. Chem. Soc.*, 2005, **127**, 11204–11205 ; J. Alauzun, E. Besson, A. Mehdi, C. Reye, R. J. P. Corriu, *Chem. Mater.*, 2008, **20**, 503–513.
24 R. Besnard, J. Cambedouzou, G. Arrachart, O. Diat, S. Pellet-Rostaing, *Langmuir*, 2013, **29**, 10368–10375.
25 Y. Li, R. Beck, T. Huang, M. C. Choi, M. Divinagracia, *J. Appl. Crystallogr.*, 2008, **41**, 1134–1139.
26 B. P. Pichon, M. Wong Chi Man, C. Bied, J. J. E. Moreau, *J. Organomet. Chem.*, 2005, 1126–1130.
27 F. Martin, A. Diran, J.-O. Durand, M. Granier, R. Desmet, *Tetrahedron Lett.*, 2005, **46**, 7973–7975.
28 A. Vrij, J. Overbeek, *J. Colloid Sci.*, 1962, **17**, 570–588.
29 S. Forster, M. Schmidt, M. Antonietti, *Polymer*, 1990, **31**, 781–792.
30 W. Schartl, C. Roos, *AIP Conference Proceedings*, 1999, **469**, 77–84.
31 (a) M. Picquart, G. Lacrampe, *Solid State Commun.*, 1987, **62**, 73–78. (b) M. Picquart, G. Lacrampe, M. Jaffrain, *Liq. Cryst.* 1990, **8**, 13–30.
32 C. J. Brinker, G. W. Scherer, Sol-Gel Science: The Physics and Chemistry of Sol-Gel Processing; Academic Press, Inc., 1990.
33 B. Riegel, S. Plittersdorf, W. Kiefer, N. Hüsing, U. Schubert, *J. Mol. Struct.*, 1997, **410**, 157–160.
34 B. Riegel, W. Kiefer, S. Hofacker, G. Schottner, *J. Sol-Gel Sci. Technol.,* 1998, **13**, 385–390.
35 R. F. Fedors, *Polym. Eng. Sci.*, 1974, **14**, 147–154.
36 Joint Committee on Powder Diffraction Standards (JCPDS) Card 34-0710.

